

Structure, composition, and defect control during plasma spray deposition of ytterbium silicate coatings

Bradley T. Richards¹ · Hengbei Zhao¹ · Haydn N. G. Wadley¹

Received: 25 June 2015 / Accepted: 14 August 2015 / Published online: 15 September 2015
© Springer Science+Business Media New York 2015

Abstract Environmental barrier coatings (EBCs) are needed to protect SiC structures exposed to high temperatures in water vapor-rich environments. Recent studies of a tri-layer EBC system consisting of a silicon layer attached to the SiC, a mullite diffusion barrier and a low-steam volatility ytterbium silicate topcoat have shown some promise for use at temperatures up to 1316 °C. However, the performance of the coating system appeared to be dependent upon the manner of its deposition. Here, an air plasma spray method has been used to deposit this tri-layer EBC on α -SiC substrates, and the effects of the plasma arc current and hydrogen content upon the structure, composition, and defects in ytterbium monosilicate (Yb_2SiO_5) and disilicate ($\text{Yb}_2\text{Si}_2\text{O}_7$) topcoats are investigated. Modification of spray parameters enabled the loss of SiO from the injected powder to be reduced, leading to partial control of coating stoichiometry and phase content. It also enabled significant control of the morphology of solidified droplets, the porosity, and the microcracking behavior within the coatings. Differences between the Yb_2SiO_5 and $\text{Yb}_2\text{Si}_2\text{O}_7$ are discussed in the context of their EBC application.

Introduction

As thermal protection concepts for superalloy components used in the most advanced gas turbine engines reach their high-temperature limits, interest has grown in the development of components made from ceramic materials with much higher maximum use temperatures [1–5]. The focus has concentrated upon damage-tolerant fiber-reinforced ceramic matrix composites (CMCs) with weak fiber/matrix interfaces. The most promising composites use boron nitride-coated SiC fibers (such as Hi-Nicalon S and Sylramic fibers) and SiC matrices incorporated by chemical vapor infiltration with residual pores filled by silicon slurry infiltration followed by carburization [5–9].

Silicon carbide ceramics react with oxygen and water vapor in combustion environments to form SiO_2 scales while releasing gaseous CO. Unfortunately, these normally protective SiO_2 scales react with water vapor at high temperatures and pressures typical of the gas turbine combustion environment, to form gaseous silicon hydroxide ($\text{Si}(\text{OH})_4$) resulting in recession of the SiC [10–15]. The rate of SiC volatilization by these mechanisms depends upon the temperature, the incident water vapor flux (pressure), and the effectiveness with which the silicon hydroxide reaction products can be removed. SiC recession rates significantly greater than 1 $\mu\text{m}/\text{h}$ can occur at gas temperatures in the 1300–1350 °C temperature range [12]. Since engine components are normally expected to survive for 5000–10,000 h of operation, silicon-containing components must be protected by coatings that inhibit these detrimental reactions. Current concepts attempt this by impeding the diffusion of oxygen and water vapor to the SiC surface using materials that are themselves resistant to volatilization. The development of these environmental barrier coatings (EBCs) for applications initially at

✉ Haydn N. G. Wadley
haydn@virginia.edu

Bradley T. Richards
btr4we@virginia.edu

Hengbei Zhao
hz5e@virginia.edu

¹ Department of Materials Science and Engineering, University of Virginia, Wilsdorf Hall, 395 McCormick Road, Charlottesville, VA 22904, USA

temperatures up to 1316 °C (but eventually 1871 °C) now paces the future use of SiC-based CMCs.

One promising EBC approach is to use a low silicon volatility material as an oxygen and water vapor diffusion barrier layer. However, its direct deposition onto SiC is not desirable because once the oxidizing species eventually diffuse through the layer, gaseous reaction products (CO) form at the SiC surface leading to a porous, low-viscosity SiO₂ scale, and high risk of coating delamination [16–18]. Instead, for applications up to 1316 °C, a sacrificial silicon layer is applied to the SiC surface first. When oxidizing species reach the silicon surface, a dense and protective SiO₂ thermally grown oxide (TGO) layer should then form, and thicken slowly (and predictably) over time [19–21]. Sometimes, mullite layers are also placed over the silicon layer to impede diffusion and mitigate potential solid-state reactions between the silicon layer and topcoat [17, 22–25]. Rare-earth silicate topcoats appear promising due to their low volatility, excellent phase stability, and reasonably well-matched coefficient of thermal expansion (CTE) with SiC substrates [23, 24, 26]. Among these, ytterbium monosilicate (Yb₂SiO₅) and ytterbium disilicate (Yb₂Si₂O₇) appear most promising due to their monomorphic nature [27], substantial prior investigation proving thermochemical stability, and viability of plasma spray deposition [23, 24, 28, 29].

Plasma spray deposition methods have been developed over a period of nearly 70 years, and are widely used to deposit a variety of surface protective coatings [30–33]. The air plasma spray (APS) process is an economical and often reliable method for the deposition of such coatings, and has attracted attention for the deposition of EBCs on SiC components [24, 25, 28, 29, 34–38]. This is a logical extension to its already widespread use for the deposition of the thermal barrier coating (TBC) systems used to protect superalloy components in current gas turbine engines [39–44]. However, preliminary studies of tri-layer ytterbium monosilicate/mullite/silicon EBCs have shown a significant sensitivity of the coating's steam cycling durability to the composition, structure, and various defects incorporated into the layers during APS deposition [28, 29]. Interest is therefore growing in the relationships between plasma spray deposition conditions and the composition, structure, and defect populations of the coating layers.

The fundamental interactions of interest in APS processing are those between the plasma spray parameters, the thermal and jet flow characteristics of the plasma plume, the composition and size distribution of the injected particles, chemical interactions with the surrounding atmosphere, and the substrate surface roughness and temperature during deposition. These interactions have been studied extensively for APS deposition via both

simulation and experiment [45–67]. Such studies have clearly established that increasing the direct arc current and secondary gas (H₂) concentration increases the peak temperature within the plasma plume and thus that experienced by powder particles as they propagate through the plume. They also increase the plasma plume's velocity, which results in a decreased particle residence time in the plasma, moderating the effect of the higher heating rate on particle temperature. Changes to the standoff distance between the exit of the plasma jet forming nozzle and the substrate also change a particle's residence time, and its velocity and temperature upon impingement with the substrate.

The particle temperature is also significantly affected by the powder size distribution and the precise trajectory taken by a particle through the plasma flow [30, 46–48, 50, 52–56, 67–69]. The APS process can therefore exhibit a substantial stochastic character; small diameter particles that take low-speed trajectories through high-temperature regions of the plasma jet may be super-heated and change composition by evaporative losses of high-vapor-pressure constituents while others may barely melt. The result is a coating containing a variety of droplet (splat) shapes and compositions after substrate impact, and the (sometimes intentional) incorporation of substantial porosity. Consequently, all of the plasma spray variables can affect the composition, microstructure, and defect populations within a coating.

Here we experimentally investigate the effects of systematically varying some of the air plasma spray deposition parameters upon the resultant composition, microstructure, and defects incorporated in the ytterbium silicate topcoats of a tri-layer ytterbium silicate/mullite/silicon EBC system applied to SiC substrates. Studies are conducted on both ytterbium monosilicate, which has a very low recession rate in steam environments [26] and upon its disilicate counterpart, which has been confirmed here to have a much closer thermal expansion coefficient to that of the α -SiC substrates.

Experimental

Powder materials

The silicon powder used for bond coat deposition was SI-122 electronics grade powder supplied by Micron Metals (Bergenfield, NJ) with a particle diameter range of 28–129 μm . The mullite (Al₆Si₂O₁₃) powder provided by Saint Gobain Ceramics (Worcester, MA) had a particle diameter of 16–53 μm . Both of the ytterbium silicate powders (Yb₂SiO₅ and Yb₂Si₂O₇) were procured from Treibacher Industrie Inc. (Toronto, ON) in fused-crushed form with irregular/angular morphology and a particle

diameter of 20–50 μm. The ytterbium silicate powders had been previously characterized and identified to be phase pure and within 1 at.% of the target stoichiometry (25 at.% Yb–12.5 at.% Si–62.5 at.% O for Yb₂SiO₅ and 18.2 at.% Yb–18.2 at.% Si–63.6 at.% O for Yb₂Si₂O₇). Both contained only minor quantities of SiO₂ and Yb₂O₃ particulates (<1 % of all particles by number, estimated to be <0.25 vol% of particulates) [29].

Plasma spray process

Tri-layer Yb-silicate/Al₆Si₂O₁₃/Si EBCs were air plasma sprayed onto 25.4 × 12.7 × 4.8 mm Hexoloy™ α-SiC substrates (Saint Gobain Ceramics, Niagara Falls, NY) using the process schematically illustrated in Fig. 1a. Substrates were prepared by lightly grit blasting one

surface with SiC to achieve an approximately 1 μm amplitude surface roughness (R_a). The substrates were ultrasonically cleaned in ethanol and inserted into a deposition fixture. The substrate-loaded fixture was then placed in a furnace set at a temperature of 1200 °C. The sample temperature was not measured during each deposition, but was during preliminary experiments which indicate that the substrate temperature varied by no more than ±100 °C as the plasma plume traversed the sample.

The high deposition temperature allowed for crystalline layers to be deposited from liquid ceramic materials that typically form amorphous compounds upon plasma spray deposition. To inhibit sample oxidation, a reducing gas composed (by volume) of 21 parts Argon to 1 part H₂ was flowed through the furnace at a rate of 20 slm. The substrates were allowed to heat for 3 min within the furnace

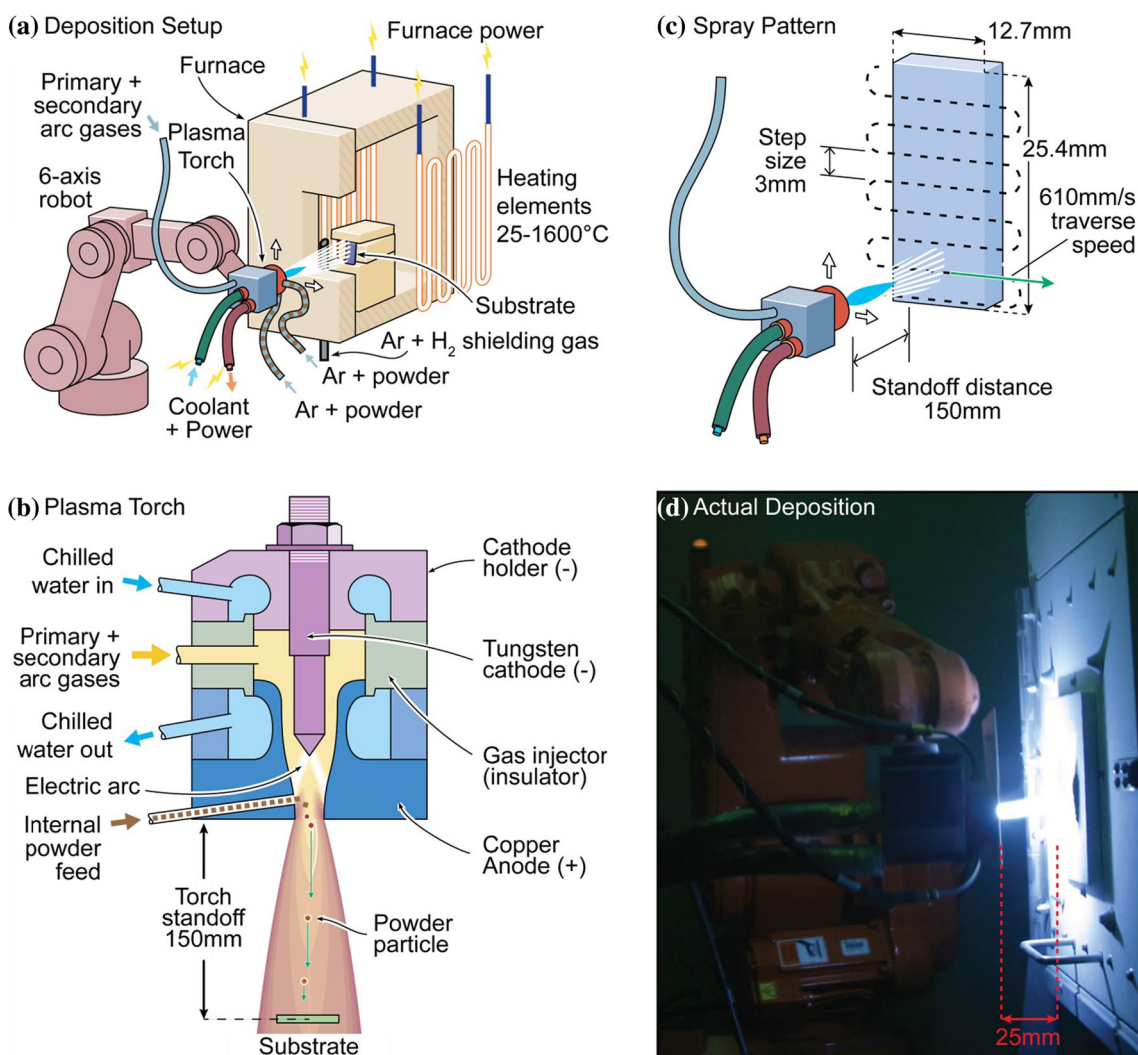


Fig. 1 **a** Schematic illustration of the air plasma spray (APS) deposition approach used for high-temperature environmental barrier coating (EBC) deposition. **b** Schematic illustration of the plasma

torch design. **c** The spray pattern and definition of relevant deposition parameters. **d** Photograph taken during APS deposition into the box furnace

with the reducing gas flowing before a front plug was removed to allow deposition to commence.

A Praxair-TAFA Model SG-100 torch with a Model 02083-175 anode configuration was used for deposition of all of the coating layers. This torch, Fig. 1b, utilized internal powder injection at 90° injection angle. It was equipped with a Model 02083-120 cathode, a Model 03083-112 gas injector, and was cooled using 10 °C chilled water with a flow rate of 30 slm. A 6-axis robot to which the APS torch was mounted traversed the ladder pattern used for deposition at constant gun to substrate standoff distance. The pattern, shown in Fig. 1c, involved 2 passes (sets) of 12 steps each of 3 mm, and was used to deposit all three coating layers. A photograph taken during deposition of an Yb₂SiO₅ coating layer using this system is presented in Fig. 1d. All the depositions utilized a torch nozzle exit to the substrate surface standoff distance of ~15 cm, while the distance from the torch to the outer front face of the furnace was ~2.5 cm.

Deposition of the Si layer was performed in the Ar/H₂ reducing gas environment furnace. Immediately after deposition of the Si layer, the reducing gas flow to the furnace was terminated and subsequent layers were then deposited. The deposition of each layer was completed in approximately 10 s (5 s per pass) and layer depositions were separated in time by only that required for the torch to change spray parameters, purge powder feed lines, and stabilize conditions for the next material (typically ~20 s). The spray parameters for deposition of the Si and Al₆Si₂O₁₃ layers are provided in Table 1.

The ytterbium silicate layers were deposited using systematically varied sets of spray parameters that had been down-selected from an initially much wider range of parameters by selecting only those that resulted in close to fully dense coatings. Four primary spray variables controlled coating composition and microstructure: (1) Powder size distribution and morphology, (2) torch standoff distance, (3) the plasma arc current, and (4) the secondary gas (H₂) concentration. Of these, the powder size distribution was fixed by the commercially available ytterbium silicate powder source. Preliminary studies indicated that reducing

the torch to substrate standoff distance beneficially affected the coating composition. However, reduction of the plasma torch standoff distance below 15 cm was physically constrained by the need for deposition onto heated substrates that resided in a thick-walled high-temperature furnace. Increasing the torch standoff distance beyond 15 cm was also discovered to increase coating porosity, and so this potential variable was held constant. As a result, only the plasma forming arc current and secondary (H₂) gas concentration were systematically investigated in the present study.

A standard “S” set of parameters was first developed that produced low pore content ytterbium silicate coatings. Subsequent coatings were then deposited using variations of parameters about this “S” spray parameter center point. The parameter combinations are listed in Table 2 with their appropriate identifying labels. Combinations of the arc current while holding all other spray parameters fixed were identified as 1C, 2C, and so on, as the current increased. Variations of the secondary H₂ gas concentration while holding all other spray parameters fixed were designated 1H, 2H, etc. The other spray parameters held constant across all depositions included the primary Ar gas flow of 84.95 slm as well as the powder carrier Ar flow of 5.90 slm for Yb₂SiO₅ and 4.72 slm for Yb₂Si₂O₇. The injected powder mass flow rate was measured using catch-can experiments. The mass flow rate for Yb₂SiO₅ was 41.5 g/min, while that of Yb₂Si₂O₇ was 35.2 g/min. Powder feed was assisted by 900 N pneumatic vibrators to ensure feed consistency. No powder pulsing was observed during deposition of any of the coating layers.

Coating characterization

The as-deposited and annealed topcoats were subjected to X-ray diffraction (XRD) measurements (X’Pert Pro MPD, PANalytical, Westborough, MA) with patterns analyzed by Rietveld refinement (HighScore Plus, PANalytical, Westborough, MA). The samples were subsequently sectioned, polished, and examined with a scanning electron microscope (Quanta 650 FE-SEM, FEI, Hillsboro, OR) operating in the back-scattered electron (BSE) mode. All images were collected under low-vacuum imaging conditions. A gamma correction was applied to enable visualization of the Yb- and non-Yb-containing materials to be simultaneously observed on all the images, and to be comparable with images in earlier works [28].

Quantitative image analysis was conducted using data collected from five randomly selected 200-μm width by 150-μm height cross-section images; the image size was sufficient to capture the full thickness of the topcoat in all spray parameter combinations. Average layer thicknesses were calculated from 50 equally spaced thickness

Table 1 Plasma spray parameters for deposition of silicon and mullite layers

APS layer	Si	Al ₆ Si ₂ O ₁₃
Arc current (A)	350	375
Primary Ar flow (slm)	77.87	77.87
Secondary H ₂ flow (slm)	0.94	0.94
Carrier Ar flow (slm)	5.90	5.43
Powder flow (g/min, port)	31.0, upper	18.9, upper
Deposition power (kW)	14.0	15.2

Table 2 Current and secondary hydrogen flows for the spray parameters used in this study to deposit the ytterbium silicate layers

Spray parameter	Current (A)	Secondary H ₂ (slm)	Power (kW) ^a	Yb ₂ SiO ₅ thickness (μm)	Yb ₂ Si ₂ O ₇ thickness (μm)
1C	225	0.94	9.3	N/A	80 ± 5
2C	250	0.94	10.3	80 ± 5	80 ± 5
S	275	0.94	11.3	80 ± 5	80 ± 5
4C	300	0.94	12.3	110 ± 5	80 ± 5
5C	325	0.94	13.3	110 ± 5	80 ± 5
1H	275	0.57	10.6	N/A	100 ± 5
2H	275	0.71	10.9	80 ± 5	80 ± 5
4H	275	1.18	11.7	80 ± 5	120 ± 5

^a Minor deviations of ±0.2 kW in spray power were observed over the course of the due to wear of torch hardware

measurements. The data from all five images was combined for quantitative metrics and taken to be a representative sample of the entire coating (having sampled a total coating layer length of approximately 10 times the coating thickness). The solidified droplet (splat) length, l to thickness, t ratio was measured for over 1000 splats for each spray parameter combination. EDS measurements of the as-deposited structures were attempted, but anomalous results were observed, leading to an inability to calculate compositions accurately by this technique. These discrepancies may have resulted from X-ray absorption and fluorescence in the Yb–Si–O system previously identified by other studies and the numerous absorption edges of the ytterbium f orbitals [70–73]. The average as-deposited compositions of ytterbium silicate layers were instead calculated from the measured volume fractions and known compositions of the phases in each of the annealed layers. The volume fractions of the phases in annealed coatings were obtained using a simple contrast threshold-crossing criterion for BSE mode images. Volume fractions were measured over 1 mm by 150 μm areas for each coating and calculated as the number of pixels of each phase divided by the total number of pixels of coating material. The analysis of phase fractions was therefore insensitive to variations in the layer thickness, porosity, and cracking.

The combination of calculated as-deposited coating stoichiometry and the BSE images of as-deposited layers allowed BSE histogram overlays on as-deposited compositional measurements. For each layer, it was assumed that the average value of the BSE histogram (value where the histogram was equally divided) corresponded to the average composition of the as-deposited layer from which the image was gathered. Further, it was assumed that in each image some area of very near stoichiometric material existed, such that the lower contrast bound of the histogram could be fixed to stoichiometric (precursor) material for all BSE images. This provides two points by which to scale the histogram in compositional space (only two points are

required for linear scaling of any shape). Such compositionally paired histograms semi-quantitatively determine the compositional *variations* between the as-deposited materials. It is noted that the BSE contrast versus ytterbium concentration curve has been calculated to be linear over most of the composition space of interest [29].

Microcrack density and orientation assessments were also performed on the as-deposited 1 mm by 150 μm wide regions of the coatings. Since the cracks had zig-zag shapes, the length and orientation of each individual linear segment of a microcrack was measured and then statistically summarized. Over 1000 individual linear crack segments were measured for each spray parameter. The data reported for microcracking are in the form of a crack areal density (CAD), defined as the length of microcrack per unit of cross-sectional area. In the present study, the CAD data are reported as length of crack (in μm) per 10,000 μm² of coating cross section. The CAD has also been analyzed as a function of angle of divergence from horizontal (the plane of the coating) for all spray parameters. From symmetry considerations, the inclination angle was reported for a single angular quadrant (0°–90° angular range), by binning in nine 10° wide increments.

Results and discussion

Tri-layer EBCs with Yb₂SiO₅/Al₆Si₂O₁₃/Si and Yb₂Si₂O₇/Al₆Si₂O₁₃/Si structure were deposited using an air plasma spray approach. Representative structures of the as-deposited tri-layer baseline (*S* parameter) coatings with ytterbium monosilicate and disilicate topcoats are shown in Fig. 2. All deposited coatings remained adherent during and after deposition and annealing. No delaminations were observed at any of the coating interfaces, particularly those surrounding the Si bond coat where delamination has previously been observed [28]. The silicon bond coat was dense when compared to those coatings deposited at low

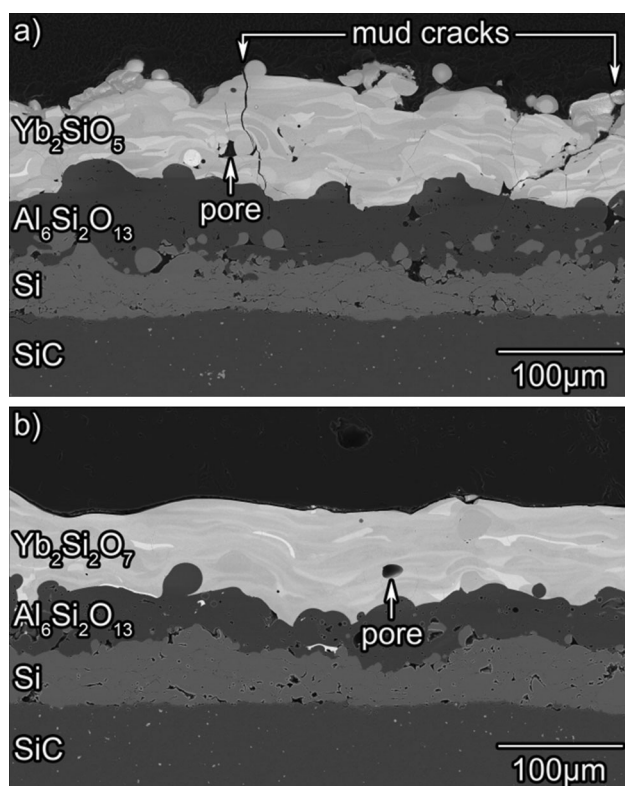


Fig. 2 The as-deposited tri-layer EBC systems deposited on a monolithic α -SiC substrate. **a** Ytterbium monosilicate and **b** ytterbium disilicate topcoats both deposited on mullite using silicon bonded substrates. The SEM images were collected in BSE mode and so the *whitest contrast phases* contained the highest concentration of the highest atomic number element (ytterbium)

temperature, and intersplat adherence was considerably improved due to a reduction in splat oxidation during deposition.

The thickness of the coatings is summarized in Table 2. All the topcoat layers were almost fully dense, with only a very small number of pores with a diameter $>10\ \mu\text{m}$ scattered randomly throughout the coatings. The density of the coating layers deposited here was higher than that of recently reported coatings deposited under very different plasma spray conditions [28]. The plasma spray parameters discussed herein were partially optimized to yield coatings of this very high density to permit the ytterbium silicates to act as a hermetic layer (vapor barrier).

Phase content

The XRD pattern of the ytterbium monosilicate coating deposited using the S combination of process parameters is shown in Fig. 3a. Analysis of the as-deposited data indicated the layer contained two monoclinic Yb_2SiO_5 phases indexed as an I2/a phase (PDF 00-040-0386) and a P21/c phase (PDF 00-052-1187), together with a cubic Yb_2O_3

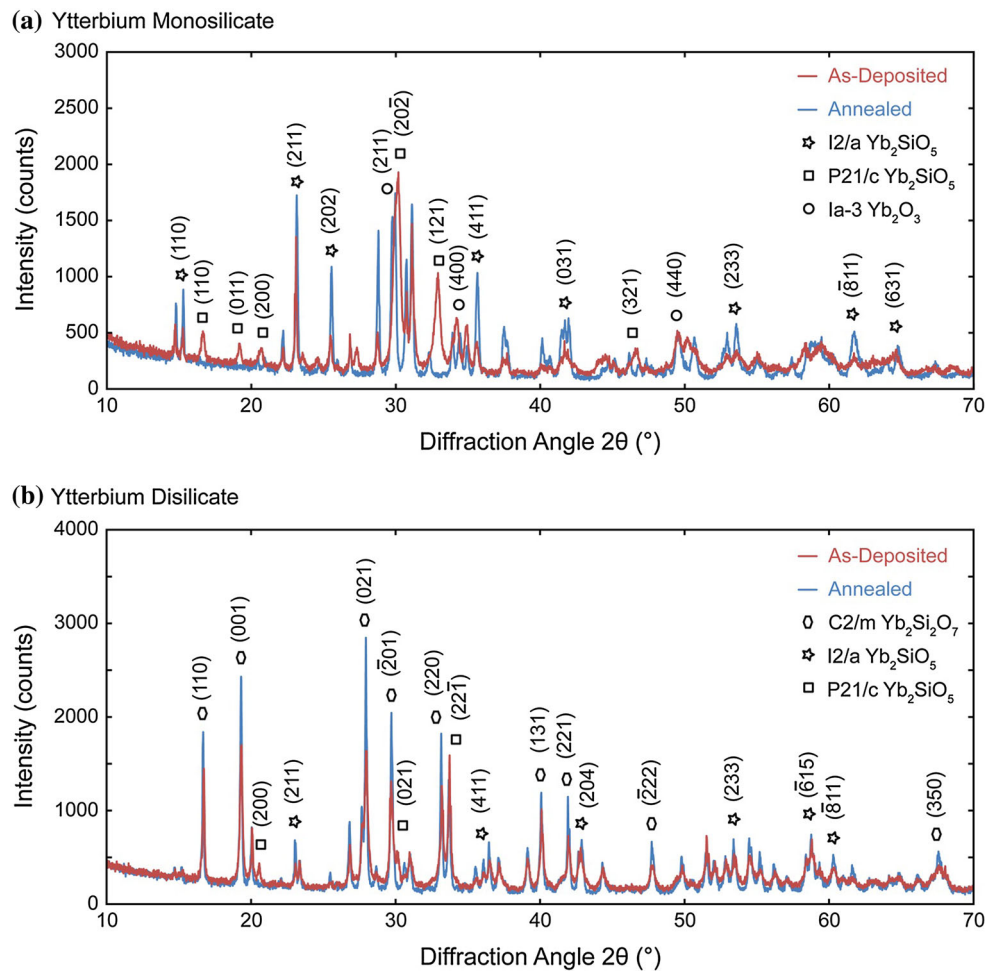
phase indexed as Ia-3 (PDF 00-041-1106). After annealing at $1300\ ^\circ\text{C}$ for 20 h, the P21/c phase almost completely disappeared, and the coating then consisted of the I2/a monoclinic phase of Yb_2SiO_5 and the cubic (Ia-3) phase of Yb_2O_3 . Rietveld analysis was unable to resolve the volume fractions of the various phases accurately due to the large number of overlapping diffraction peaks and the varying background. Qualitatively, the as-deposited ytterbium monosilicate layers had a P21/c to I2/a phase volume fraction ratio of $\sim 2:1$. Qualitatively, the relative peak intensities of the cubic ytterbia phase diffraction peaks increased with increasing deposition parameter (current and H_2 concentration) indicating an increase in volume fraction of ytterbia in the coatings. However, the volume fractions of the respective phases could not be reliably determined from the diffraction patterns of these plasma-sprayed material.

The diffraction patterns of the as-deposited and annealed ytterbium disilicate layers deposited using the S combination of processing parameters are shown in Fig. 3b. The XRD pattern of the as-deposited layer could be indexed as a mixture of C2/m monoclinic $\text{Yb}_2\text{Si}_2\text{O}_7$ (PDF 04-007-4857) and the same two phases of monoclinic Yb_2SiO_5 observed in the as-deposited ytterbium monosilicate layers (I2/a and P21/c). After annealing, only the C2/m monoclinic $\text{Yb}_2\text{Si}_2\text{O}_7$ phase and I2/a monoclinic Yb_2SiO_5 phase were observed in the coating, Fig. 3b. Again, Rietveld analyses could not be used for quantitative phase determination due to the issues mentioned above. Qualitatively, they indicated an approximately monotonic increase in the P21/c to I2/a Yb_2SiO_5 phase volume fraction ratio with plasma spray power (from a ratio of 7:2 at low deposition powers to 13:2 at the highest deposition power). After annealing, the metastable P21/c Yb_2SiO_5 phase had again transformed in all the layers. Similar to the monosilicate system, an increase in relative peak intensity of those peaks from the Yb_2SiO_5 I2/a phase was observed with increasing deposition power in annealed coatings, indicating increased volume fraction of the monosilicate.

Observations of the ytterbium silicate layers using BSE mode SEM imaging revealed regions of light and dark contrast in the ytterbium silicate layers, Fig. 2. The light regions have been previously shown to correspond to solidified particle droplets that are ytterbium rich (Si-depleted) compared to the stoichiometric powder material [28, 29]. Only the darkest gray regions in the images had a Si content close that of the stoichiometric powder. Examinations of the two topcoats at higher magnifications revealed the compositional variations to be quite severe, Fig. 4.

In as-deposited layers observed in the SEM at relatively low magnification, Fig. 4a, d, a broad spectrum of contrast was observed indicative of a continuous range of

Fig. 3 X-ray diffraction patterns of the as-deposited and annealed topcoats. **a** Ytterbium monosilicate and **b** ytterbium disilicate both deposited using the S combination of deposition parameters



compositions. However, there are only four equilibrium phases (including the two terminal compounds) in the Yb_2O_3 – SiO_2 pseudo-binary phase diagram at temperatures up to 1750 $^\circ\text{C}$: the two pure terminal oxides, Yb_2SiO_5 , and $\text{Yb}_2\text{Si}_2\text{O}_7$ [27, 73]. The continuous variation of contrast in the two topcoats was found to not correspond to multiple intermediate phases, but rather from variations in the fractions of the extremely fine-grained Yb_2O_3 , Yb_2SiO_5 , and $\text{Yb}_2\text{Si}_2\text{O}_7$ line compounds simultaneously sampled by the electron beam [29]. This is supported by XRD analyses indicating the presence of only these three compounds in the two materials in either their as-deposited or annealed condition. The very fine crystal size in the as-deposited structure is consistent with the rapid quench rate of the APS process and slow crystallization kinetics of compounds with large unit cells.

After stabilization annealing, only two different contrast phases were observed in BSE micrographs, Fig. 4 (annealed micrographs b and e). These phases correspond to those observed in X-ray diffraction: I2/a Yb_2SiO_5 and Ia-3 Yb_2O_3 in the ytterbium monosilicate layers, and C2/m $\text{Yb}_2\text{Si}_2\text{O}_7$ and I2/a Yb_2SiO_5 in the ytterbium disilicate

layers. The volume fraction of a second phase that formed in an individual splat upon annealing varied in accordance with the stoichiometry of the splat during deposition, Fig. 4b and e. As a result, prior splat boundaries were “visible” in many images based upon differences in the volume fraction of their phases despite the lack of an actual physical boundary, Fig. 4c and f. High-magnification imaging indicated a heterogeneous distribution of second-phase precipitates on a fine scale and revealed the grain structure of the layer, Fig. 4c and f. The slight grain-to-grain variations in contrasts within the two phases in Fig. 4c and f may be a result of variations in electron channeling with orientation (“band contrast”), not of compositional variation.

FIB lift-outs from annealed S spray parameter ytterbium monosilicate and ytterbium disilicate layers were analyzed using transmission electron microscopy to verify the precise phases observed in XRD, Figs. 5 and 6. In TEM bright field imaging, the contrast of the phases are reversed from SEM BSE imaging since they are transmission and not back-scattered electron mode images. Thus, Yb-rich regions appear darker in contrast than Si-rich material in

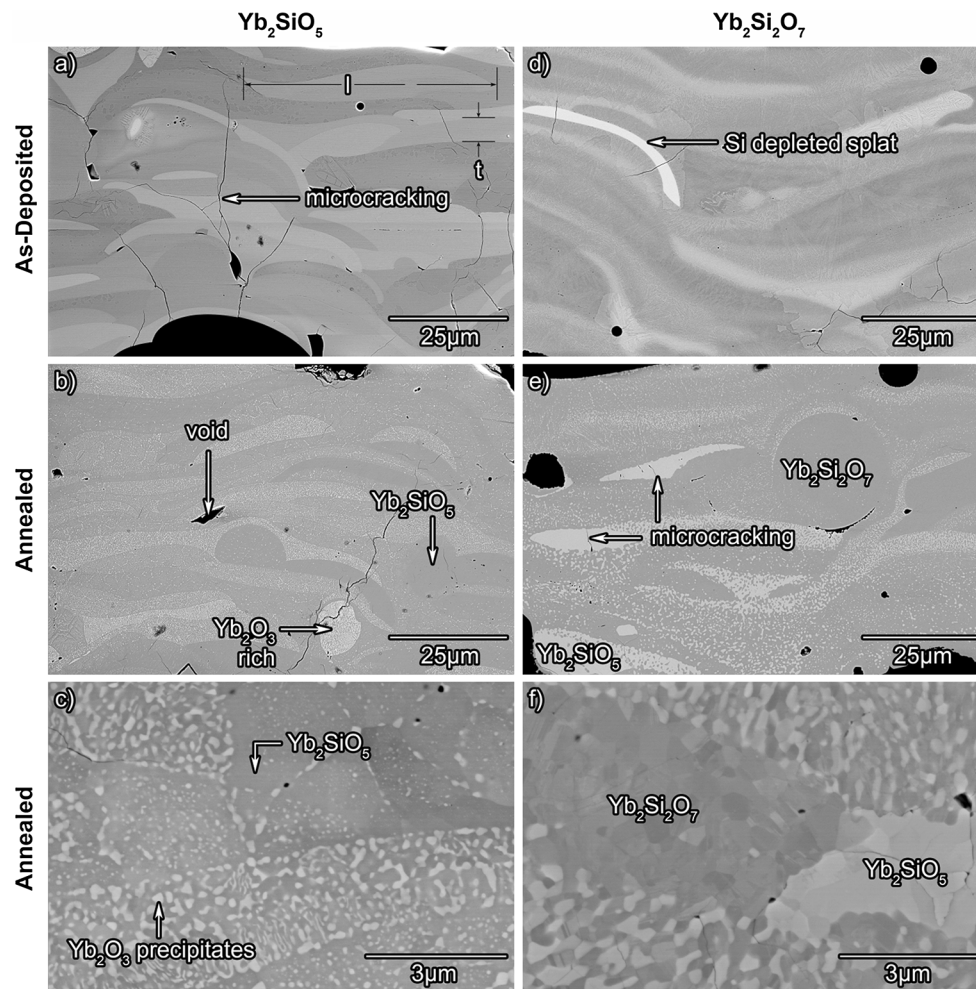


Fig. 4 BSE mode SEM micrographs of the ytterbium silicate layers deposited using the S combination of deposition parameters. **a** As-deposited, **b** annealed, and **c** high-magnification annealed ytterbium

monosilicate layer. **d–f** Correspond to as-deposited, annealed, and high-magnification annealed ytterbium disilicate layers

TEM micrographs. Bright field imaging of the ytterbium monosilicate layer, Fig. 5a, revealed a structure that was reflective of that in Fig. 4c. EDS measurements of the composition of the two phases (at probe locations indicated by crosses in Fig. 5d) revealed compositions very close to Yb_2O_3 for the precipitated phase and Yb_2SiO_5 for the matrix, Table 3. Selected area electron diffraction (SAED) was used in the area indicated in Fig. 5a to capture diffraction patterns of the matrix phase on two different zone axes, Fig. 5b and c. Indexing of these diffraction patterns identified the structure as monoclinic I2/a Yb_2SiO_5 , Table 4. The shape and structure of the precipitates was generally equiaxed, Fig. 5a and d. The SAED pattern of the precipitate from Fig. 5d was indexed as cubic Yb_2O_3 , Fig. 5e. Additional low-intensity diffraction spots were evident in the pattern of Fig. 5e resulting from overlap of the beam with neighboring Yb_2SiO_5 grains.

Analogous analyses were performed on an ytterbium disilicate coating deposited using the S-parameter combination, Fig. 6. Bright field imaging indicated the layer to be multiphase (as in Fig. 4d–f) with several large matrix-phase grains suitable for analysis in a FIB lift-out sample, Fig. 6. Again, high-magnification bright field imaging was used to capture the physical structure of precipitated particles and the matrix-precipitate interface, Fig. 6b. The EDS compositions measured at the probe points marked by crosses in Fig. 6b aligned closely with the compositions of $\text{Yb}_2\text{Si}_2\text{O}_7$ and Yb_2SiO_5 , Table 3. SAED patterns from the spot in Fig. 6a were analyzed for two different zone axes, Fig. 6c and d, and indexed as monoclinic C2/m $\text{Yb}_2\text{Si}_2\text{O}_7$, Table 4. SAED analyses were also performed upon the precipitates, and indexed diffraction patterns conform to those given in Table 4 for Yb_2SiO_5 . These analyses indicate that air plasma spray deposition from stoichiometric

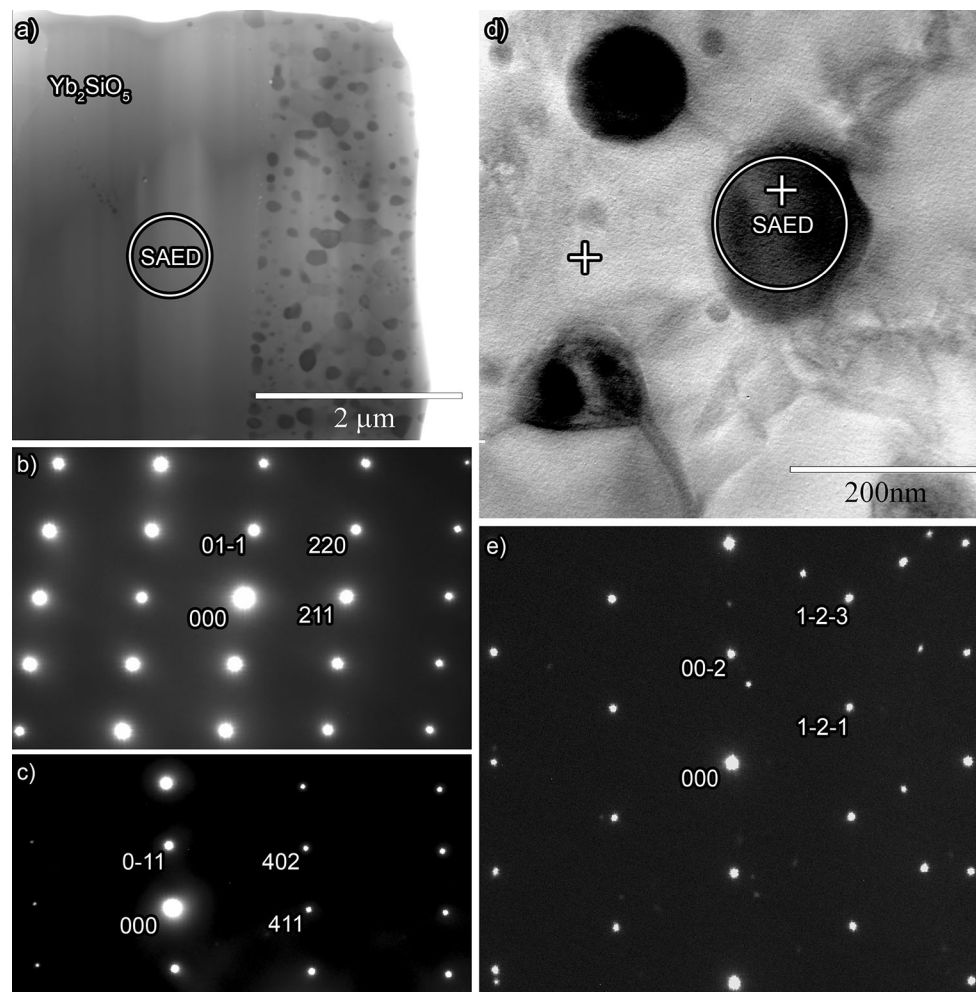


Fig. 5 **a** Bright field TEM image of the ytterbium monosilicate coating. **b** The $[111]$ and **c** the $[122]$ selected area electron diffraction (SAED) zone axis patterns from the monoclinic Yb_2SiO_5 phase.

d High-magnification bright field image of the precipitated phase in the Yb_2SiO_5 matrix. **e** Shows the cubic Yb_2O_3 precipitate diffraction pattern along the $[210]$ zone axis

composition powder has resulted in Si-depleted, mixed-phase coating layers.

The average volume of precipitated phase in annealed coatings was calculated as a function of deposition parameter for all ytterbium silicate layers, Fig. 7. The trends and relative magnitudes of Fig. 7 were found to agree with the semi-quantitative data calculated from diffraction patterns of the annealed layers, corroborating the validity of the image analysis measurements. In ytterbium monosilicate layers, Fig. 7a, the volume fraction of precipitated Yb_2O_3 followed a monotonically increasing trend with deposition power as either the plasma current or H_2 concentration were varied (while holding other deposition parameters constant). The minimum volume fraction of precipitated Yb_2O_3 was ~ 8 vol% in the 2H coating and the maximum was ~ 16 vol% in the 5C coating as the plasma spray power was varied over a range of only 3.0 kW. In ytterbium disilicate coatings, the volume

fraction of Yb_2SiO_5 also followed a monotonically increasing trend with plasma current, Fig. 7b. The volume fraction of precipitated Yb_2SiO_5 in ytterbium disilicate layers ranged from ~ 9 vol% for the 1H coating to ~ 24 vol% for the 5C coating. The volume fraction of the precipitated phase in ytterbium disilicate coatings could be changed by ~ 15 vol% as the deposition power was varied over a range of 4.5 kW.

To summarize, while the powder particles used to deposit both ytterbium silicate layers were single phase and of stoichiometric composition, BSE imaging contrast of deposited microstructures revealed the presence of Yb_2O_3 precipitate particles in Yb_2SiO_5 coatings and Yb_2SiO_5 particles in the $\text{Yb}_2\text{Si}_2\text{O}_7$ coatings. Such precipitated phases have been previously observed in plasma-sprayed ytterbium silicates [23, 24, 28, 29]. Both precipitates were Si-deficient in comparison to the matrix (and initial powder) phase. The crystal structures and compositions,

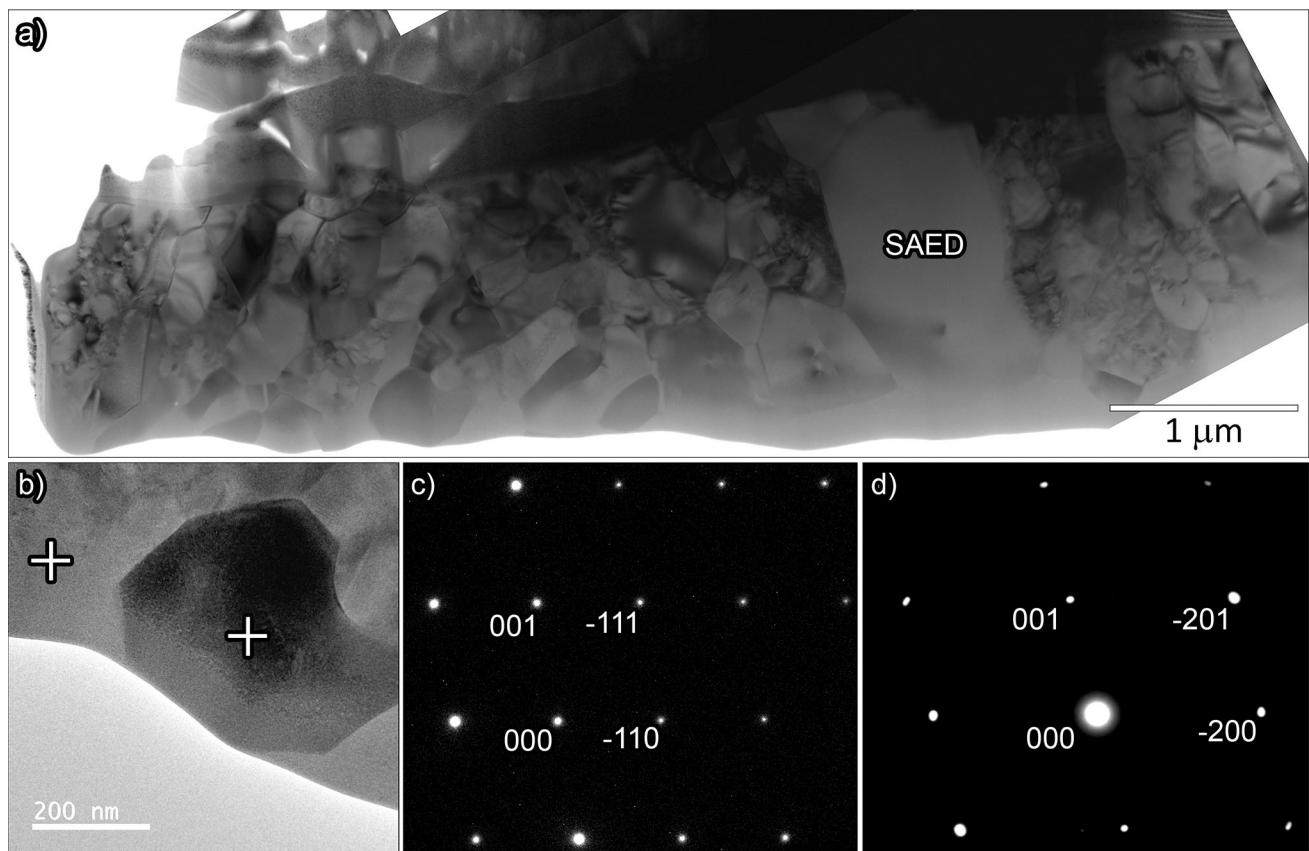


Fig. 6 **a** Bright field TEM image of the ytterbium disilicate coating and **b** high-magnification bright field image of a precipitated Yb_2SiO_5 particle. Crosses indicate the locations of EDS probes for characterizing the matrix and precipitate phases. **c** The [110] and **d** the [010]

selected area electron diffraction patterns along zone axes of monoclinic $\text{Yb}_2\text{Si}_2\text{O}_7$ from the region indicated by SAED circled in **a**

Table 3 Chemical compositions of the precipitated particles and matrix in the annealed coatings

Composition (at.%)	O	Yb	Si
Precipitate in Yb_2SiO_5	60.0	38.1	1.9
Matrix of Yb_2SiO_5	62.8	24.3	12.9
Stoichiometric Yb_2SiO_5	62.5	25.0	12.5
Precipitate in $\text{Yb}_2\text{Si}_2\text{O}_7$	63.2	23.0	13.8
Matrix of $\text{Yb}_2\text{Si}_2\text{O}_7$	62.6	17.6	19.8
Stoichiometric $\text{Yb}_2\text{Si}_2\text{O}_7$	63.6	18.2	18.2

Table 4 Lattice constants calculated from diffraction patterns and PDF cards

Lattice source	a (Å)	b (Å)	c (Å)	β (°)
Yb_2SiO_5 PDF ^a	12.38	6.67	10.29	102.54
Yb_2SiO_5 SAED	12.63	6.70	10.53	105.56
$\text{Yb}_2\text{Si}_2\text{O}_7$ PDF ^b	6.80	8.87	4.70	102.12
$\text{Yb}_2\text{Si}_2\text{O}_7$ SAED	6.78	8.42	4.73	100.48

^a PDF card (00-040-0386)

^b PDF card (04-007-4857)

Figs. 3, 5, and 6 and Tables 2 and 3, are consistent with the binary phase diagram predictions [27]. Despite appropriate stoichiometry and reported monomorphism [27], a monoclinic P21/c Yb_2SiO_5 phase was observed in both ytterbium monosilicate and ytterbium disilicate layers. This phase was not present in annealed coatings, as indicated in the diffraction patterns of Fig. 3, indicating the P21/c Yb_2SiO_5 phase to be metastable and transformable to the stable monoclinic I2/a phase of Yb_2SiO_5 .

Splat aspect ratio

Variation of the spray parameters resulted in changes to the solidified droplet structures of the as-deposited ytterbium monosilicate coatings, Fig. 8, and ytterbium disilicate coatings, Fig. 9. In both Figs. 8 and 9, the spray deposition power increased from a–c to d–b. Figures 8 and 9a and b correspond to the lowest and highest power used in the plasma direct arc current variation study, whereas parts c

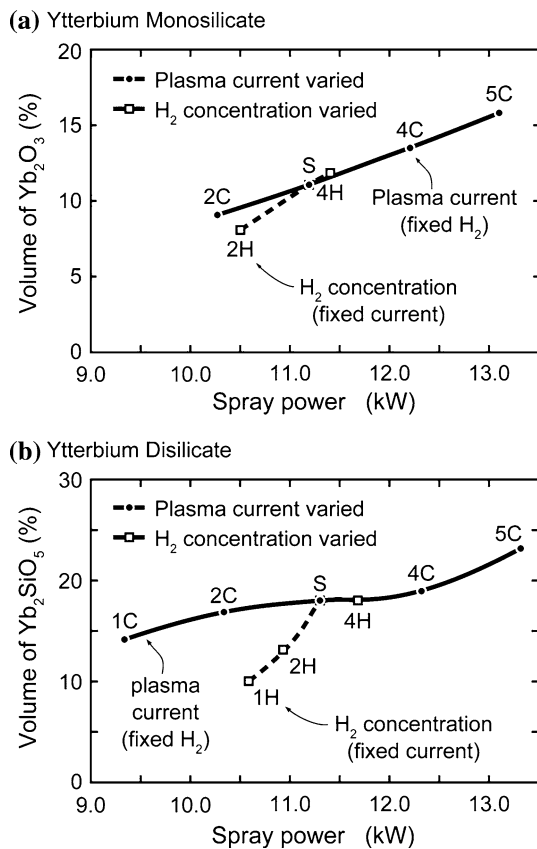


Fig. 7 Volume fraction of second-phase precipitates in annealed coatings plotted against plasma spray power. **a** Yb_2O_3 precipitated in ytterbium monosilicate coatings. **b** Yb_2SiO_5 precipitated in ytterbium disilicate coatings

and d corresponded to the lowest and highest power used in the H_2 variation study. Very fine nano-grain structures were visible in all of the coatings. The prevalence of large, round, unmelted particles also decreased with increasing deposition power in both materials. Variation of the process conditions caused changes to the splat length, l , its thickness, t , and the splat aspect ratio (l/t). Increasing the plasma current or the plasma plume H_2 concentration (while maintaining other spray parameters constant) resulted in an increase of splat l/t ratio, Fig. 10. The splat l/t ratio ranged from ~ 4 to ~ 17 for ytterbium monosilicate layers and from ~ 7 to ~ 14 for the ytterbium disilicate layers. The data indicate that though variation of both plasma current and H_2 concentration monotonically increase the splat aspect ratio, the effect was not simply governed by spray power alone. As indicated in “Coating characterization” section, it is apparent in Figs. 8 and 9 that partially melted particles (of near stoichiometric composition) exist in all coating layers as a consequence of variations in particle trajectories within the plasma plume.

Particles that had both high temperature and velocity during impingement with the substrate are expected to

flatten the most and thus result in splats that had the highest aspect ratio. It is noted that both higher velocity and temperature result from increased plasma current and/or secondary gas concentration [30, 32, 47, 48, 52–56, 69, 74, 75], but the entire temperature–time–velocity (T – t – V) history is important in determining splat microstructure. These process parameters have also affected the loss of silicon, Fig. 11 (and accordingly the volume fraction of second-phase precipitate, Fig. 9), and the splat aspect ratio, Fig. 10, in similar ways. Detailed plasma plume modeling and simulations are now necessary to quantify these aspects of the study.

Coating composition

Since EDS estimates of the coating composition were found to be unreliable, the average composition of the as-deposited ytterbium silicate layers was calculated from volume fractions of the precipitated line compound phases and their stoichiometric compositions in annealed coatings. This relationship was calculated from molar volumes and densities of the Yb_2O_3 , Yb_2SiO_5 , and $\text{Yb}_2\text{Si}_2\text{O}_7$ phases, and is shown for the ytterbium silicate systems in Fig. 11a. Since the volume fractions of the phases in each coating were known, Fig. 7, it was then possible to estimate the effect of deposition conditions upon the average Yb:Si ratio of the two types of coating, Fig. 11b and c. There was a significant increase in the Yb:Si ratio of both types of coatings as the plasma spray power was increased.

BSE mode imaging of annealed coatings indicated significant differences in grayscale contrast between the splats. The BSE grayscale was then mapped to the mole fraction of the elements in the as-deposited microstructures by rescaling a BSE contrast histogram to known reference points (as described in “Coating characterization” section) to obtain BSE-derived distributions of Yb:Si ratio. This was achieved by aligning the lowest Yb:Si ratio (darkest BSE contrast) end of the histogram with the stoichiometry of the lowest equilibrium Yb:Si compound in the system,¹ and the distributions average with that deduced from the phase volume fractions, Fig. 11b and c. Such a scaling assumed that some stoichiometric material remained in the coatings after deposition and that the BSE contrast scaled linearly with Yb:Si ratio. The BSE-derived distributions show that a significant increase in splat composition range also accompanied the average stoichiometric shift with an increase in the plasma spray power and plasma hydrogen content.

To understand the reasons for the loss of silicon in the coatings, equilibrium vapor pressure calculations were

¹ For Yb_2SiO_5 , the stoichiometric Yb:Si ratio is 2 and for the $\text{Yb}_2\text{Si}_2\text{O}_7$ this stoichiometric ratio is 1.

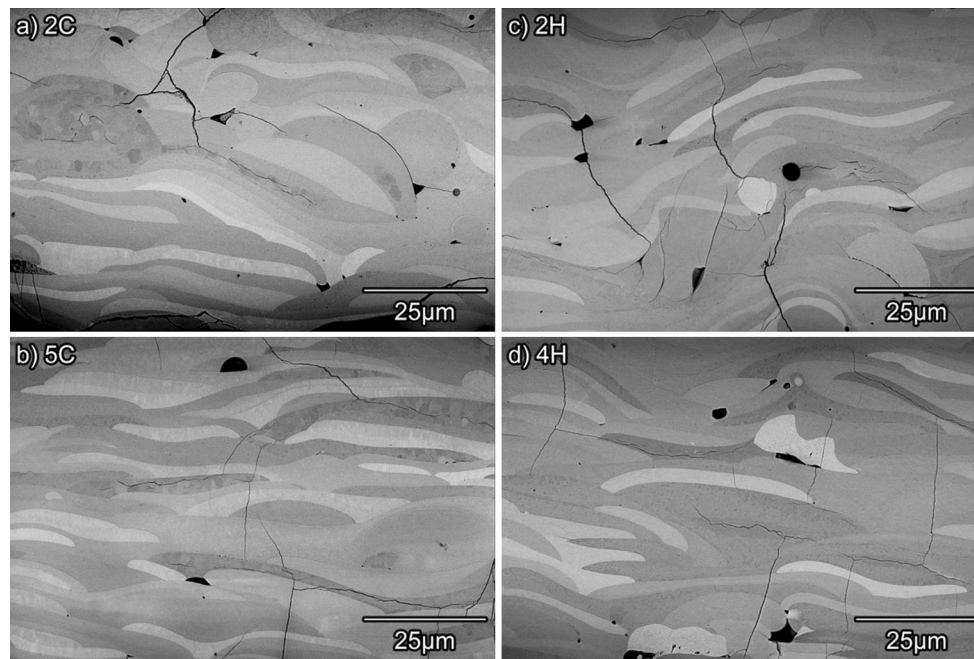


Fig. 8 BSE mode SEM micrographs of the as-deposited ytterbium monosilicate coatings deposited using different combinations of spray parameters. **a** 2C coating, **b** 5C coating, **c** 2H coating, and **d** 4H coating

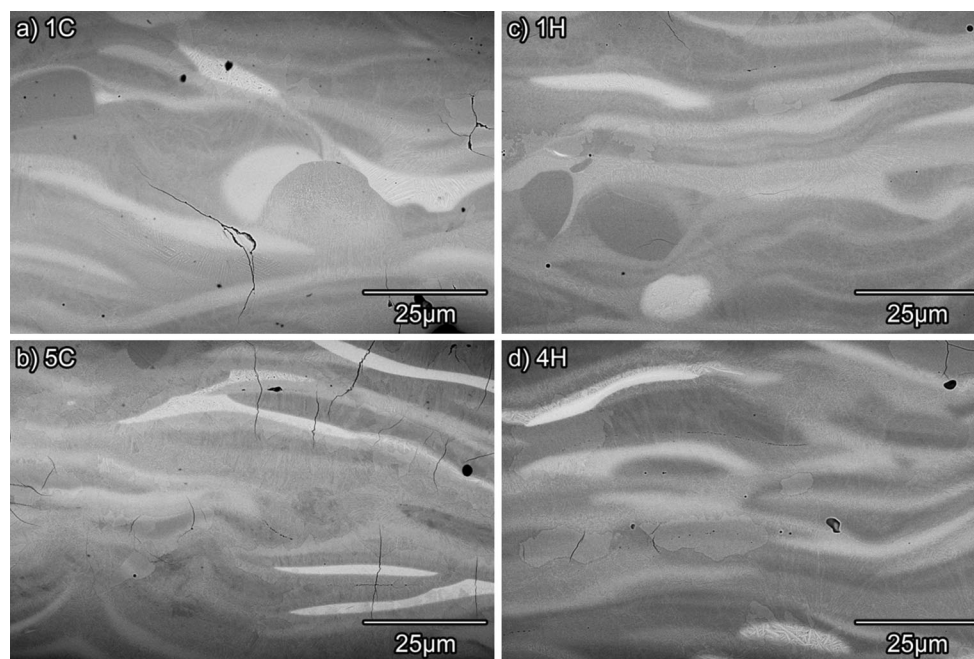


Fig. 9 BSE mode SEM micrographs of the as-deposited ytterbium disilicate coatings deposited using different combinations of spray parameters. **a** 1C coating, **b** 5C coating, **c** 1H coating, and **d** 4H coating

performed using FactSage [76] thermochemical modeling software in conjunction with the FactPS database. All modeling of the Yb–Si–O system used ideal solution interaction calculations since no published thermochemical data for this system exists. Vapor partial pressures and

partial pressure ratios in the Yb–Si–O system were calculated over the temperature interval of 1000–3000 °C that could be experienced by a powder particle during plasma spray deposition. Figure 12a shows the vapor pressures of the dominant vapor species (normalized by the vapor

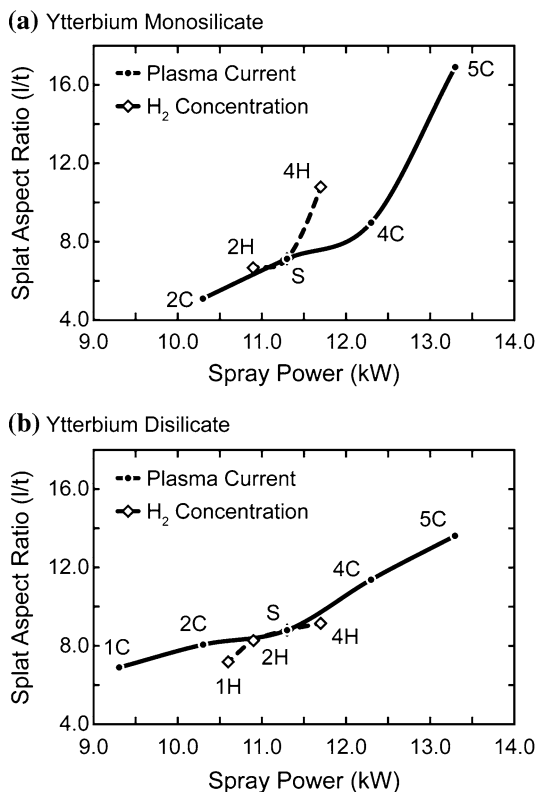


Fig. 10 Variations in average splat aspect ratio (*l/t*) as a function of plasma spray power for **a** ytterbium monosilicate and **b** ytterbium disilicate coatings in the as-deposited condition

pressure of SiO) for a system consisting of 0.0914 mol of Yb_2SiO_5 (0.0457 mol Yb_2O_3 + 0.0457 mol SiO_2), 4.057 mol Ar, 0.042 mol H_2 , and 4.5×10^{-7} mol O_2 corresponding to S spray parameter mass flows during ytterbium monosilicate deposition. The significant SiO partial pressure resulted from the decomposition (reduction) of SiO_2 . Figure 12b shows recalculations for ratios of $\text{Yb}_2\text{Si}_2\text{O}_7$ ($\text{Yb}_2\text{O}_3 + 2\text{SiO}_2$), Ar, H_2 , and O_2 appropriate for the S spray parameter mass flows of the ytterbium disilicate coating depositions. Figure 12c plots the ideal solution predicted partial vapor pressures of the highest partial pressure Si-bearing and Yb-bearing vapor species of the S spray parameter for both Yb_2SiO_5 and $\text{Yb}_2\text{Si}_2\text{O}_7$. The vertical dashed line marked in all three plots of Fig. 12 indicates the temperature above which all Si would be in vapor form.

In the Yb_2SiO_5 system, Fig. 12a, the vapor pressure calculated for SiO was $\sim 10^6$ times greater than that of Yb for temperatures below 2500 °C. At temperatures above 2500 °C, the ratio decreased, but was still roughly 10^2 times higher than that of Yb at 3000 °C. SiO_2 vapor, the secondary Si-bearing species, had a vapor partial pressure ratio to SiO that varied from $\sim 10^{-7}$ at 1000 °C to $\sim 10^{-1}$ at 2500 °C, decreasing to $\sim 10^{-2}$ at 3000 °C. The partial

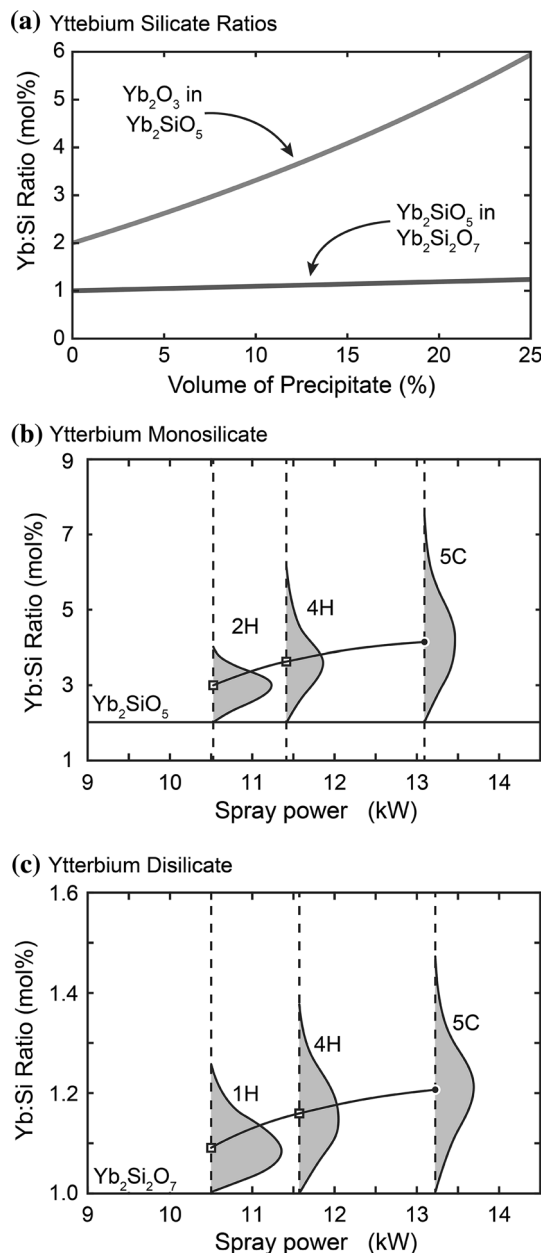


Fig. 11 a Yb:Si ratio dependence upon molar volume of second phases. The average Yb to Si ratios and BSE contrast estimates of the composition variation in **b** the ytterbium monosilicate and **c** the ytterbium disilicate layers. BSE-derived distributions were scaled by aligning the lowest Yb:Si ratio (*darkest BSE contrast*) end of the distribution with the stoichiometric compound and enforcing the average of the distribution to match that deduced from the phase volume fractions

pressures of both H_2O and OH were relatively high, with H_2O having a partial pressure comparable to SiO between 1200 and 2500 °C, before gradually decline as the temperature was further increased. The OH partial pressure varied between $\sim 10^{-2}$ and $\sim 10^{-4}$ of the SiO partial pressure across the entire temperature range. The $\text{Yb}_2\text{Si}_2\text{O}_7$

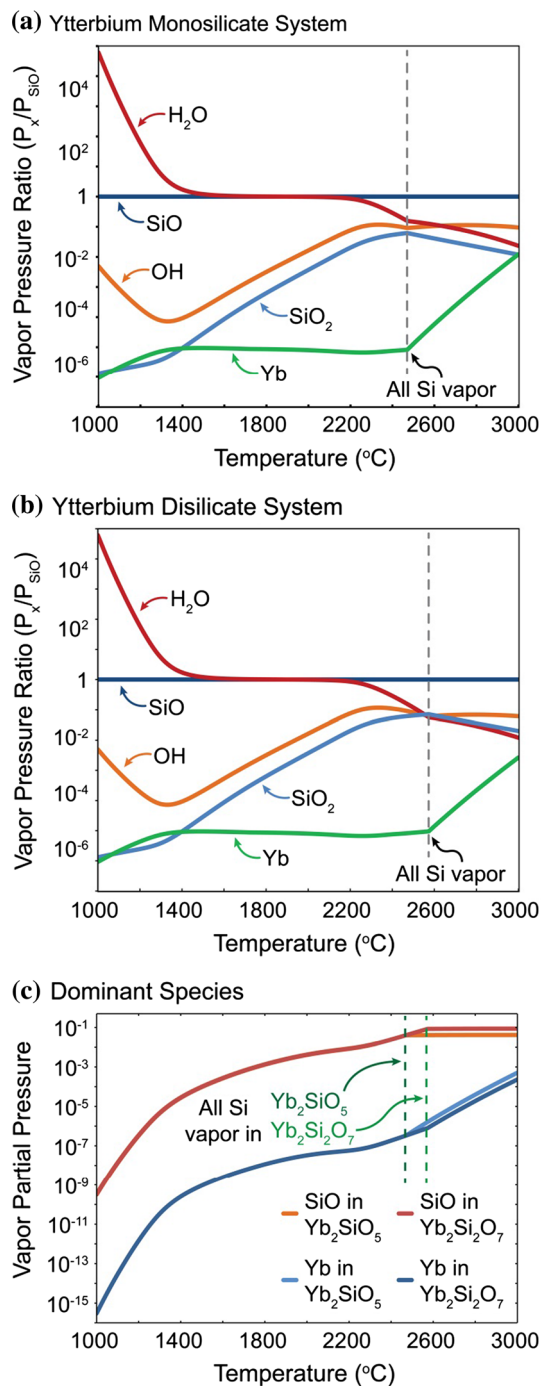


Fig. 12 Partial pressure of dominant vapor species scaled to that of SiO as a function of temperature for the S spray parameter condition. **a** Yb_2SiO_5 and **b** $Yb_2Si_2O_7$. **c** Shows the calculated vapor partial pressures of dominant species. Partial pressures are calculated based on ideal thermochemical interactions

system, Fig. 12b, behaved almost identically to that of Yb_2SiO_5 . There was a slight difference in the Yb and SiO_2 curves above 2500 °C, wherein the difference in partial pressures between SiO and Yb was slightly larger (by a factor of 10) and the difference in partial pressures between

SiO and SiO_2 was slightly smaller (again by a factor of 10) when compared to the Yb_2SiO_5 system.

Additional calculations were conducted using a thermochemical database for the Si–O–H–Yb system recently developed by Opila [77] which includes data for the hydroxides. Using the molar masses of the materials in the plasma plume (including the range of H_2 contents), the vapor pressure versus temperature relations for all the species that could form were calculated including the hydroxides of SiO such as $SiO(OH)_2$ and $Si(OH)_4$ and the OH and H_2O pressures. The silicon hydroxide partial pressures were of order 10^{-6} lower than that of SiO; a consequence of insufficient water vapor in the plume (formed by the reaction of H_2 with O formed because of decomposition of SiO_2 to form SiO). These results indicated that the reaction of H_2 with the other constituents of the system did not change the SiO partial pressure for any of the H_2 fractions used in the study.

The predicted values of vapor partial pressures for SiO and Yb for the two systems are shown in Fig. 12c. The calculated vapor pressures of both species exhibited a sharp increase over four orders of magnitude between 1000 and 1400 °C. This increase was followed by a gradual rise of roughly two orders of magnitude between 1400 and 2500 °C. Above 2500 °C, the vapor pressures of SiO in the two systems remained constant at $\sim 10^{-1}$ (all Si was in vapor form as denoted) while those of Yb increased to $\sim 10^{-4}$. Over the 1000–3000 °C temperature interval, the SiO partial pressure varied from $\sim 10^{-10}$ to $\sim 10^{-1}$ and the Yb partial pressure varied from $\sim 10^{-16}$ to $\sim 10^{-4}$. It is emphasized that the results should be interpreted only qualitatively as the analysis was based upon ideal interactions. As such, the calculations are insensitive to differences between Yb_2SiO_5 and $Yb_2Si_2O_7$ (such differences have been calculated in the Y–Si–O system using real thermochemical data) [74]. In summary, the calculations demonstrate the existence of a significant driving force for preferential loss of Si (compared to Yb) from molten material during particle propagation through a high-temperature plasma plume.

Implications of silica depletion

A combination of air plasma spray parameters has been identified that resulted in the deposition of low-porosity ytterbium monosilicate and ytterbium disilicate layers on silicon and mullite-coated α -SiC substrates. However, the low-porosity coatings were Si-depleted compared to the (near stoichiometric) composition of the starting powders. BSE mode imaging indicated that the degree of Si depletion varied from solidified droplet to droplet in a given coating, Figs. 2, 4, 8, and 9. This compositional variability increased with spray power. The average composition of

the coatings was also increasingly depleted in Si with increase in the plasma spray arc current and the hydrogen content of the plasma plume, Figs. 7 and 11.

The loss of silicon was consistent with preferential volatilization of Si-bearing species from melted powder during transit through the plasma plume. Ideal solution thermochemical modeling indicated that Si-bearing species had vapor pressures that were $\sim 10^6$ times higher than Yb-bearing species at the temperatures likely to have been reached during APS deposition of both the ytterbium monosilicate, Fig. 12a, and the ytterbium disilicate, Fig. 12b. This vapor pressure ratio difference also remained relatively constant across a temperature range from ~ 1300 to 2600 °C. Rapid Si depletion during powder particle transit through the plume was driven by the high Si-bearing species vapor pressure, Fig. 12c, which increased with increasing temperature in a manner consistent with the observed loss of Si with increasing deposition power, Figs. 7 and 11. Reducing the plasma temperature (by decreasing the plasma power and H_2 concentration) and particle residence time in the plume (by shortening the standoff distance and increasing the particle velocity) provides a means for reducing the silicon loss, but at the risk of increased porosity.

The volume fraction of precipitate in both ytterbium silicate layers increased with both increasing plasma current and H_2 concentration, Fig. 7. This occurs because increases in these spray parameters increased the temperatures of the plasma plume, and therefore the rate of silicon loss. This in turn increased precipitate fraction (by application of the lever rule to the Yb_2O_3 – SiO_2 binary phase diagram). While increasing the plasma current and secondary gas (H_2) concentration both increased the precipitate fraction, the effects of modifying these variables were not equal. This was clearly indicated by the difference in the slope of the precipitate phase volume fraction versus plasma current and H_2 concentration curves in Fig. 7.

The high silicon loss during plasma deposition of the rare-earth silicates such as the ytterbium silicate system studied here makes it challenging to apply low-porosity (dense) ytterbium silicate microstructures via APS processing and will require careful selection and control of spray parameters. The challenges to the deposition of coatings for EBC applications are compounded by the formation of extensive mud cracking (providing high-permeability oxygen and water vapor pathways to the underlying layers) in the ytterbium monosilicate system. While mud cracks are not formed in the disilicate material, loss of silicon leads to the formation of ytterbium monosilicate regions that are susceptible to microcracking upon cooling. If such cracks are retained on reheating, they are likely to reduce the effectiveness of the topcoat resistance to oxygen and steam permeation. However, if the volatility could be

controlled, it may permit fabrication of coatings containing layers of varying phase fraction from a single stoichiometric powder composition. This might provide an ability to tailor the thermophysical properties of ytterbium silicate coatings or develop graded coatings by modification of APS deposition parameters.

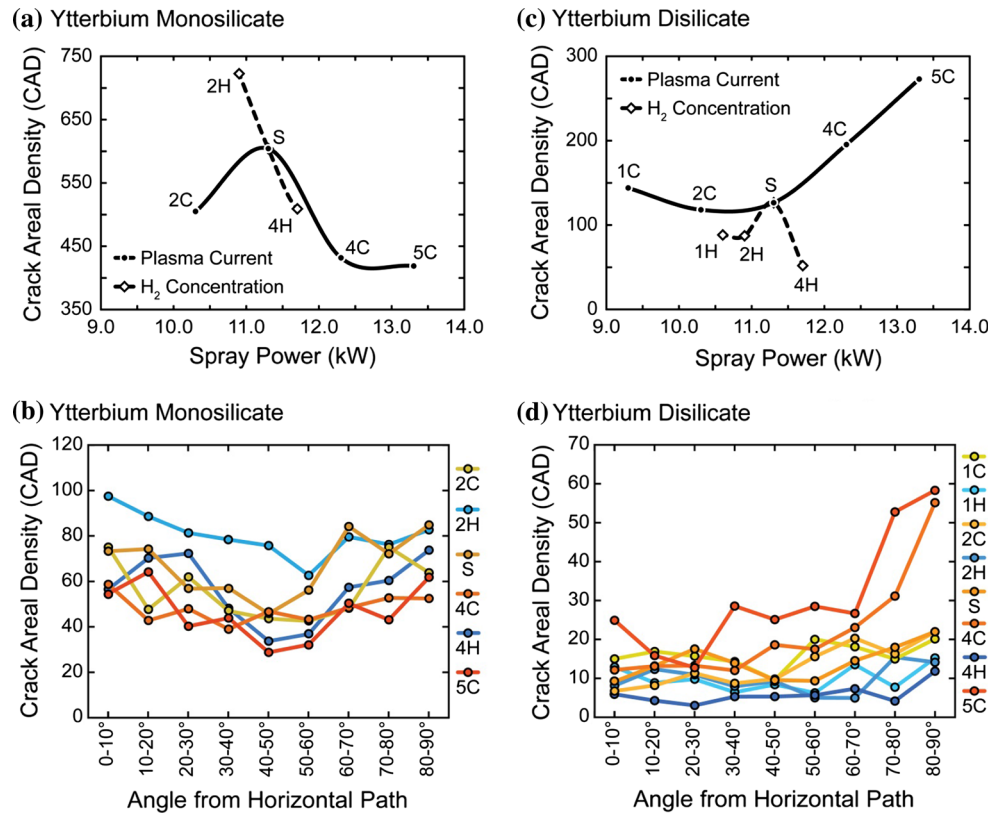
Channel-type and equiaxed microcracking

Significant channel (mud)-type cracking was observed in ytterbium monosilicate coatings, Fig. 2a. The inter-crack spacing was ~ 240 μm , and resulted from the coating's substantially higher coefficient of thermal expansion (CTE) compared to that of the substrate (7.5×10^{-6} °C $^{-1}$ for ytterbium monosilicate compared to 4.7×10^{-6} °C $^{-1}$ for SiC) [23, 29]. These cracks fully penetrated the layer but their spacing did not vary with spray power. No mud cracking was observed in ytterbium disilicate layers. Dilatometer experiments (reported in Appendix) with this material confirmed that it has a similar CTE to the SiC substrate. Both ytterbium silicate coatings also contained numerous microcracks. This microcracking was significantly affected by spray conditions used to deposit the ytterbium silicate layers, Fig. 13. The total microcrack length per unit area generally decreased with increasing spray power used to deposit the ytterbium monosilicate layers, Fig. 13a. This trend was consistent with the increase in the coatings' Yb_2O_3 fraction (decrease in Yb_2SiO_5) with spray power, Fig. 7. The variation in crack angle (defined from the plane of the coating) for the ytterbium monosilicate microcracks is shown in Fig. 13b for each of the deposition conditions. The microcrack angle was almost random; only a slight preference for high-angle (90° , i.e., micro-channel crack type) crack orientations was observed.

The microcrack length per unit area in the ytterbium disilicate layers was significantly less than that of ytterbium monosilicate layers, Fig. 13c. It generally tended to increase with spray power as the fraction of the high CTE Yb_2SiO_5 phase increased, Fig. 7. The crack length distribution as a function of angle from horizontal for the ytterbium disilicate layers is shown in Fig. 13d. Like the ytterbium monosilicate system, the orientation angle of ytterbium disilicate microcracks in most of the coatings was random. However, the coatings deposited at the highest spray powers (4C and 5C layers) had many more vertically oriented cracks, consistent with the presence of a higher fraction of the higher CTE Yb_2SiO_5 phase.

Channel-type (mud) cracks were observed to penetrate fully the ytterbium monosilicate layers of the tri-layer coating system when deposited on a SiC substrate, Fig. 2a. However, no cracks of this type were found in the ytterbium disilicate coating system, Fig. 2b. Furthermore, the mud crack spacing in the ytterbium monosilicate layers

Fig. 13 Crack areal density (CAD) of ytterbium silicate layers: microcrack length (in μm) per $10,000 \mu\text{m}^2$ of coating cross section. **a** Crack length of all orientations plotted as a function of plasma spray power for the ytterbium monosilicate layers. **b** Crack length as a function of angle of divergence from horizontal crack path in ytterbium monosilicate layers. A 90° angle indicates vertical (mud crack type) cracking. The plots in **c** and **d** are similar data for ytterbium disilicate layers (note the scale change)



was not found to depend upon the spray parameters (within statistical margins). The results are consistent with previous studies which attributed the mud cracking to the development of tensile residual stress in the ytterbium monosilicate layer during cooling dictated by CTE [23, 24, 28, 29]. Earlier dilatometry studies found that the CTE of ytterbium monosilicate was $7.5 \times 10^{-6} \text{ }^\circ\text{C}^{-1}$, [23, 29] approximately twice that of the SiC and sufficient to develop an in-plane biaxial tensile stress approaching 1 GPa. The measured CTE for ytterbium disilicate (Appendix) confirmed that the disilicate layer has a CTE of $\sim 4.1 \times 10^{-6} \text{ }^\circ\text{C}^{-1}$, slightly less than that of SiC and consistent with the absence of mud cracking.

In addition to the mud cracks in the ytterbium monosilicate system, equiaxed microcracks were found in all the layers of both topcoat materials; a finding with potentially significant consequences for the rate of permeation of oxidizing species to the bond coat. In ytterbium monosilicate layers, the microcracking was severe and varied considerably with deposition parameter, Fig. 13a. The angular distribution of microcracks in the ytterbium monosilicate layer was generally random and was unaffected by spray parameter, Fig. 13b. The equiaxed microcracking was associated with regions of the highest ytterbia content, but the reason for this is presently unclear since ytterbium oxide has both a similar Young's elastic modulus

(171 GPa) and CTE ($7.6 \times 10^{-6} \text{ }^\circ\text{C}^{-1}$) compared to the surrounding ytterbium monosilicate phase (172 GPa and $7.5 \times 10^{-6} \text{ }^\circ\text{C}^{-1}$), and therefore a similar stored elastic strain energy to drive microcracking [29].

In ytterbium disilicate, the extent of microcracking was greatly reduced, Fig. 13c. The most severely cracked ytterbium disilicate layer had $\sim 40\%$ lower crack density than the least severely cracked ytterbium monosilicate layer. Microcracks in the ytterbium disilicate layers usually had a random angular distribution indicative of equiaxed cracking. However, the two ytterbium disilicate layers subjected to the hottest plasma deposition conditions (4C and 5C) had $\sim 3\text{--}4$ times the density of high-angle orientation ($70^\circ+$ from horizontal) cracks, but with no change in low-angle microcrack population, Fig. 13d. Microstructural analysis indicated this crack distribution to be an additional population of micro-mud cracks within precipitated Yb_2SiO_5 particles. The presence of such cracking in only the ytterbium disilicate 4C and 5C coatings resulted from the increased Yb_2SiO_5 volume fraction in these layers. Microcracking of such precipitates is consistent with a local state of tension upon cooling due to the difference in CTE between $\text{Yb}_2\text{Si}_2\text{O}_7$ ($4.1 \times 10^{-6} \text{ }^\circ\text{C}^{-1}$) and Yb_2SiO_5 ($7.5 \times 10^{-6} \text{ }^\circ\text{C}^{-1}$) [23, 29]. The vertical nature of this cracking resulted from the high l/t ratio and in-plane orientation of the large precipitates combined with the biaxial

nature of the stress field in the relatively thin ytterbium disilicate layer.

Conclusions

Low-porosity ytterbium monosilicate and ytterbium disilicate coatings have been deposited using an air plasma spray approach. The dependence of the microstructure, composition, and microcracking of these coatings was examined for a variety of spray parameters that resulted in close to fully dense coatings. It has been found that

- Air plasma spray deposition of low-porosity ytterbium mono- and disilicate layers on silicon and mullite-coated SiC substrates has been shown to be possible over a wide range of plasma spray conditions using powders with a particle diameter of 20–50 μm .
- The deposition of ytterbium monosilicate layers on silicon and mullite-coated silicon carbide substrates resulted in substantial mud (channel) cracking perpendicular to the coating surface and randomly oriented microcracking. The mud cracks penetrated the entire thickness of the ytterbium monosilicate layer, and were formed because of the substantially higher CTE of the ytterbium monosilicate compared to that of the substrate. The equiaxed cracks appeared to result from local variations in splat composition and therefore elastic modulus and CTE.
- Low-porosity ytterbium disilicate layers contained no mud cracks and exhibited less equiaxed microcracking than the monosilicate. Thermal dilatometry measurements indicated the bulk material had a CTE of approximately $4.1 \times 10^{-6} \text{ }^\circ\text{C}^{-1}$, close to that of the SiC substrates. The elimination of mud cracking, and reduction of microcracking, indicates that rapid pathways for the permeation of oxidizing species in this material may be reduced.
- The high partial vapor pressure of SiO at elevated temperature resulted in substantial loss of silicon from the originally stoichiometric powder during air plasma spraying. The silicon depletion in deposited layers varied considerably within each coating due to the variation of temperature, particle trajectory, and residence in the plasma plume. The average coating composition and compositional range of the as-deposited splats were also strongly affected by the spray deposition parameters.
- The high volatility of Si led to precipitation of Yb_2O_3 in the ytterbium monosilicate coatings and Yb_2SiO_5 in the ytterbium disilicate layers. The crystal structures were verified as equilibrium phases

and their lattice parameters measured using selected area electron diffraction (SAED) during TEM analysis. A metastable monoclinic Yb_2SiO_5 was observed in both ytterbium monosilicate layers and ytterbium disilicate layers, but this phase transformed to the equilibrium monoclinic Yb_2SiO_5 crystal structure during annealing.

- Variation of the deposition parameter had significant effects on phase fractions, splat aspect ratio, total length of microcrack observed, and orientation of microcracking in both ytterbium silicates.

Acknowledgements The authors would like to acknowledge Elizabeth Opila and Jeroen Deijkers of the University of Virginia for assistance and helpful discussions related to the Factsage modeling and Bryan Harder of the NASA Glenn Research Center. This work was supported by the Office of Naval Research under Grant N00014-11-1-0917 managed by Dr. David Shiffler.

Appendix: Thermal expansion of ytterbium disilicate

The thermal expansion coefficient (CTE, α) of $\text{Yb}_2\text{Si}_2\text{O}_7$ has been measured for 95 % dense spark plasma-sintered (SPS) ytterbium disilicate, Fig. 14. The SPS blank was machined to $25 \times 5 \times 5$ mm in dimension and was lightly diamond polished to remove surface imperfections and to square edges. The resulting dilatometry specimen was annealed in lab air at 1400 $^\circ\text{C}$ for 100 h prior to testing to establish oxygen stoichiometry in the material after sintering.

X-ray diffraction pole figures were produced for the dilatometry specimen to assess its crystallographic texture. The pole figures indicated no crystallographic texture in the dilatometry specimen. XRD patterns confirmed the specimen to be monoclinic ytterbium disilicate with no other phases discernible. Dilatometry was performed using a

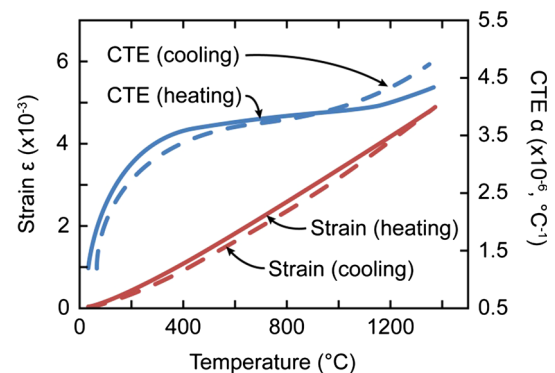


Fig. 14 Thermal strain and expansion coefficient of 100 h annealed 95 % dense spark plasma-sintered (SPS) ytterbium disilicate

Netsch (Burlington, MA) 402-C dilatometer using high-purity α -alumina as a calibration standard. Heating and cooling ramp rates were 0.05 °C/s. Slight hysteresis was observed in the heating and cooling curves of the specimen, Fig. 14, but did not invalidate the CTE measurement.

References

- Ohnabe H, Masaki S, Onozuka M, Miyahara K, Sasa T (1999) Potential application of ceramic matrix composites to aero-engine components. *Compos A* 30(4):489–496
- Tressler RE (1999) Recent developments in fibers and interphases for high temperature ceramic matrix composites. *Compos A* 30(4):429–437
- Naslain R, Christin F (2003) SiC-matrix composite materials for advanced jet engines. *MRS Bull* 28(9):654–658
- Igawa N, Taguchi T, Nozawa T, Snead LL, Hinoki T, McLaughlin JC, Katoh Y, Jitsukawa S, Kohyama A (2005) Fabrication of SiC fiber reinforced SiC composite by chemical vapor infiltration for excellent mechanical properties. *J Phys Chem Solids* 66(2-4):551–554
- Evans AG, Marshall DB (1989) Overview no. 85 The mechanical behavior of ceramic matrix composites. *Acta Metall* 37(10):2567–2583
- Evans AG, Zok FW, Davis J (1991) The role of interfaces in fiber-reinforced brittle matrix composites. *Compos Sci Technol* 42(1-3):3–24
- Marshall DB, Evans AG (1985) Failure mechanisms in ceramic-fiber/ceramic-matrix composites. *J Am Ceram Soc* 68(5):225–231
- Rühle M, Evans AG (1989) High toughness ceramics and ceramic composites. *Prog Mater Sci* 33(2):85–167
- DiCarlo JA, Yun H-M, Morscher GN, Bhatt RT (2005) SiC/SiC composites for 1200 C and above. In: Bansal NP (ed) *Handbook of ceramic composites*. Kluwer Academic Publishers, Boston, pp 77–98
- Costello JA, Tressler RE (1986) Oxidation kinetics of silicon carbide crystals and ceramics: I, in dry oxygen. *J Am Ceram Soc* 69(9):674–681
- Opila EJ (1999) Variation of the oxidation rate of silicon carbide with water-vapor pressure. *J Am Ceram Soc* 82:625–636
- Opila EJ (2003) Oxidation and volatilization of silica formers in water vapor. *J Am Ceram Soc* 86:1238–1248
- Opila EJ, Fox DS, Jacobson NS (1997) Mass spectrometric identification of Si-O-H(g) species from the reaction of silica with water vapor at atmospheric pressure. *J Am Ceram Soc* 80:1009–1012
- Opila EJ, Hann RE Jr (1997) Paralineer oxidation of CVD SiC in water vapor. *J Am Ceram Soc* 80:197–205
- Opila EJ, Smialek JL, Robinson RC, Fox DS, Jacobson NS (1999) SiC recession caused by SiO₂ scale volatility under combustion conditions: II, thermodynamics and gaseous-diffusion model. *J Am Ceram Soc* 82:1826–1834
- Lee KN (1998) Contamination effects on interfacial porosity during cyclic oxidation of mullite-coated silicon carbide. *J Am Ceram Soc* 81:3329–3332
- Lee KN (2000) Key durability issues with mullite-based environmental barrier coatings for Si-based ceramics. *J Eng Gas Turbines Power* 122:632–636
- Lee KN, Miller RA (1996) Development and environmental durability of mullite and mullite/YSZ dual layer coatings for SiC and Si₃N₄ ceramics. *Surf Coat Technol* 86–87:142–148
- Deal BE (1963) The oxidation of silicon in dry oxygen, wet oxygen, and steam. *J Electrochem Soc* 110:527–533
- Deal BE, Grove AS (1965) General relationship for the thermal oxidation of silicon. *J Appl Phys* 36:3770–3778
- Razouk RR, Lie LN, Deal BE (1981) Kinetics of high pressure oxidation of silicon in pyrogenic steam. *J Electrochem Soc* 128:2214–2220
- Lee KN (2000) Current status of environmental barrier coatings for Si-based ceramics. *Surf Coat Technol* 133–134:1–7
- Lee KN (2006) Protective coatings for gas turbines. In: Dennis R (ed) *The gas turbine handbook*. United States Department of Energy (DOE), Wasington
- Lee KN, Fox DS, Bansal NP (2005) Rare earth silicate environmental barrier coatings for SiC/SiC composites and Si₃N₄ ceramics. *Corros Ceram Matrix Compos* 25:1705–1715
- Lee KN, Fox DS, Eldridge JI, Zhu D, Robinson RC, Bansal NP, Miller RA (2003) Upper temperature limit of environmental barrier coatings based on mullite and BSAS. *J Am Ceram Soc* 86:1299–1306
- Jacobson NS, Fox DS, Smialek JL, Dellacorte C, Lee KN (2005) Performance of ceramics in severe environments. In: Cramer SD, Covino BS (eds) *ASM handbook*. NASA Glenn Research Center (GRC), Cleveland
- Bondar IA (1982) Rare-earth silicates. *Ceram Int* 8:83–89
- Richards BT, Begley MR, Wadley HNG (2015) Mechanisms of ytterbium monosilicate/mullite/silicon coating failure during thermal cycling in water vapor. *J Am Ceram Soc*. doi:10.1111/jace.13792
- Richards BT, Wadley HNG (2014) Plasma spray deposition of tri-layer environmental barrier coatings. *J Eur Ceram Soc* 34(12):3069–3083
- Pfender E (1988) Fundamental studies associated with the plasma spray process. *Surf Coat Technol* 34:1–14
- Singh H, Sidhu BS, Puri D, Prakash S (2007) Use of plasma spray technology for deposition of high temperature oxidation/corrosion resistant coatings—a review. *Mater Corros* 58(2):92–102
- Zaaf JH (1983) A quarter of a century of plasma spraying. *Annu Rev Mater Sci* 13:9–42
- McPherson R (1981) The relationship between the mechanism of formation, microstructure and properties of plasma-sprayed coatings. *Thin Solid Films* 83(3):297–310
- Faber KT, Weyant CM, Harder B, Almer J, Lee K (2007) Internal stresses and phase stability in multiphase environmental barrier coatings. *Int J Mater Res* 98:1188–1195
- Harder BJ, Almer J, Lee KN, Faber KT (2009) In situ stress analysis of multilayer environmental barrier coatings. *Powder Diffr* 24:94–98
- Lee KN (2006) Protective coatings for gas turbines. National Energy Technology Laboratory (NETL), Pittsburgh
- Lee KN, Eldridge JI, Robinson RC (2005) Residual stresses and their effects on the durability of environmental barrier coatings for SiC ceramics. *J Am Ceram Soc* 88:3483–3488
- Richards BT, Ghosn LJ, Zhu D, Wadley H (2015) Mechanical properties of air plasma sprayed environmental barrier coating (EBC) systems: preliminary assessments. In: *Proceedings of the 39th international conference and exposition on advanced ceramics and composites*
- Rabiei A, Evans AG (2000) Failure mechanisms associated with the thermally grown oxide in plasma-sprayed thermal barrier coatings. *Acta Mater* 48(15):3963–3976
- Miller RA (1997) Thermal barrier coatings for aircraft engines: history and directions. *J Therm Spray Tech* 6(1):35–42
- Schlichting KW, Padture NP, Jordan EH, Gell M (2003) Failure modes in plasma-sprayed thermal barrier coatings. *Mater Sci Eng A* 342(1-2):120–130

42. Choi SR, Hutchinson JW, Evans AG (1999) Delamination of multilayer thermal barrier coatings. *Mech Mater* 31:431–447
43. Lee CH, Kim HK, Choi HS, Ahn HS (2000) Phase transformation and bond coat oxidation behavior of plasma-sprayed zirconia thermal barrier coating. *Surf Coat Technol* 124(1):1–12
44. Zhu D, Miller RA (2000) Thermal conductivity and elastic modulus evolution of thermal barrier coatings under high heat flux conditions. *J Therm Spray Tech* 9(2):175–180
45. Lugscheider E, Nickel R, Papenfuß-Janzen N (2004) A model of the interface between plasma jet simulation and the simulation of coating formation during atmospheric plasma spraying (APS). *J Phys IV* 120:373–380
46. Meillot E, Balmigere G (2008) Plasma spraying modeling: particle injection in a time-fluctuating plasma jet. *Surf Coat Technol* 202(18):4465–4469
47. Remesh K, Yu SCM, Ng HW, Berndt CC (2003) Computational study and experimental comparison of the in-flight particle behavior for an external injection plasma spray process. *J Therm Spray Tech* 12(4):508–522
48. Streibl T, Vaidya A, Friis M, Srinivasan V, Sampath S (2006) A critical assessment of particle temperature distributions during plasma spraying: experimental results for YSZ. *Plasma Chem Plasma Process* 26(1):73–102
49. Trelles JP, Heberlein JVR (2006) Simulation results of arc behavior in different plasma spray torches. *J Therm Spray Tech* 15(4):563–569
50. Vardelle M, Fauchais P, Vardelle A, Li KL, Dussoubs B, Thémelis NJ (2001) Controlling particle injection in plasma spraying. *J Therm Spray Tech* 10(2):267–284
51. Vardelle M, Vardelle A, Fauchais P, Moreau C (1994) Pyrometer system for monitoring the particle impact on a substrate during a plasma spray process. *Meas Sci Technol* 5(3):205
52. Wang P, Yu SCM, Ng HW (2004) Particle velocities, sizes and flux distribution in plasma spray with two powder injection ports. *Mater Sci Eng A* 383(1):122–136
53. Williamson RL, Fincke JR, Chang CH (2000) A Computational examination of the sources of statistical variance in particle parameters during thermal plasma spraying. *Plasma Chem Plasma Process* 20(3):299–324
54. Williamson RL, Fincke JR, Chang CH (2002) Numerical study of the relative importance of turbulence, particle size and density, and injection parameters on particle behavior during thermal plasma spraying. *J Therm Spray Tech* 11(1):107–118
55. Xiong H-B, Zheng L-L, Sampath S, Williamson RL, Fincke JR (2004) Three-dimensional simulation of plasma spray: effects of carrier gas flow and particle injection on plasma jet and entrained particle behavior. *Int J Heat Mass Transf* 47(24):5189–5200
56. Zhang T, Gawne DT, Liu B (2000) Computer modelling of the influence of process parameters on the heating and acceleration of particles during plasma spraying. *Surf Coat Technol* 132(2–3):233–243
57. Chang C (1992) Numerical simulation of alumina spraying in argon-helium plasma jet. Presented at the 1992 International Thermal Spray Conference, Orlando, FL, 1–5 Jun 1992, vol 1, pp 1–5
58. He MY, Hutchinson JW, Evans AG (2003) Simulation of stresses and delamination in a plasma-sprayed thermal barrier system upon thermal cycling. *Mater Sci Eng A* 345(1–2):172–178
59. Li H-P, Chen X (2001) Three-dimensional simulation of a plasma jet with transverse particle and carrier gas injection. *Thin Solid Films* 390(1–2):175–180
60. Ramachandran K, Kikukawa N, Nishiyama H (2003) 3D modeling of plasma–particle interactions in a plasma jet under dense loading conditions. *Thin Solid Films* 435(1–2):298–306
61. Ramachandran K, Nishiyama H (2004) Fully coupled 3D modeling of plasma–particle interactions in a plasma jet. *Thin Solid Films* 457(1):158–167
62. Trelles JP, Chazelas C, Vardelle A, Heberlein JVR (2009) Arc plasma torch modeling. *J Therm Spray Technol* 18(5–6):728–752
63. Vardelle M, Vardelle A, Fauchais P, Boulos MI (1983) Plasma-particle momentum and heat transfer: modelling and measurements. *AIChE J* 29(2):236–243
64. Moreau C, Cielo P, Lamontagne M, Dallaire S, Vardelle M (1990) Impacting particle temperature monitoring during plasma spray deposition. *Meas Sci Technol* 1(8):807
65. Liu H, Lavernia EJ, Rangel RH (1993) Numerical simulation of substrate impact and freezing of droplets in plasma spray processes. *J Phys D* 26(11):1900
66. Mostaghimi J, Pasandideh-Fard M, Chandra S (2002) Dynamics of sput formation in plasma spray coating process. *Plasma Chem Plasma Process* 22(1):59–84
67. Li H-P, Pfender E (2007) Three dimensional modeling of the plasma spray process. *J Therm Spray Technol* 16(2):245–260
68. Friis M, Persson C, Wigren J (2001) Influence of particle in-flight characteristics on the microstructure of atmospheric plasma sprayed yttria stabilized ZrO₂. *Surf Coat Technol* 141(2–3):115–127
69. Srinivasan V, Friis M, Vaidya A, Streibl T, Sampath S (2007) Particle injection in direct current air plasma spray: salient observations and optimization strategies. *Plasma Chem Plasma Process* 27(5):609–623
70. Yamamoto T, Tanaka T, Matsuyama T, Funabiki T, Yoshida S (1999) XAFS study of the structure of the silica-supported ytterbium oxide catalyst. *Solid State Commun* 111(3):137–142
71. Van Loon JC, Galbraith JH, Aarden HM (1971) The determination of yttrium, europium, terbium, dysprosium, holmium, erbium, thulium, ytterbium and lutetium in minerals by atomic-absorption spectrophotometry. *Analyst* 96(1138):47–50
72. Dragic PD, Carlson CG, Croteau A (2008) Characterization of defect luminescence in Yb doped silica fibers: part I NBOHC. *Opt Express* 16(7):4688–4697
73. Felsche J (1973) The crystal chemistry of the rare-earth silicates. Rare earths, vol 13. Springer, Berlin, pp 99–197
74. Dyshlovenko S, Pawlowski L, Roussel P, Murano D, Le Maguer A (2006) Relationship between plasma spray operational parameters and microstructure of hydroxyapatite coatings and powder particles sprayed into water. *Surf Coat Tech* 200(12–13):3845–3855
75. Janisson S, Meillot E, Vardelle A, Coudert JF, Pateyron B, Fauchais P (1999) Plasma spraying using Ar-He-H₂ gas mixtures. *J Therm Spray Tech* 8(4):545–552
76. Bale CW, Chartrand P, Degterov SA, Eriksson G, Hack K, Ben Mahfoud R, Melançon J, Pelton AD, Petersen S (2002) FactSage thermochemical software and databases. *Calphad* 26(2):189–228
77. Opila E (2015) Private communication of unpublished thermochemical data. University of Virginia, Virginia